Check for updates

RESEARCH ARTICLE

ADVANCED MATERIALS INTERFACES Open Access

www.advmatinterfaces.de

Electromechanical Anisotropy in Aligned Nanomesh Electrodes for E-Skin Applications

Hyeokjin Cho, Gaeun Yun, Phuong Thao Le, Tae Sik Hwang, Juhyeong Jeon, Seung Whan Kim, Jungho Lee, and Geunbae Lim**

Electrospun nanomesh electrodes offer excellent mechanical conformity and breathability for skin-integrated electronics. However, conventional randomly oriented structures exhibit isotropic behavior, limiting functional adaptability. Here, a geometry-driven approach is presented to achieve electromechanical anisotropy by aligning fibers within free-standing, monolayer nanomesh electrodes. Through parylene vapor coating and gold evaporation, devices are fabricated that respond distinctly when strained parallel or perpendicular to the fiber alignment. Under parallel strain, the mesh undergoes direct fiber elongation and gold fracture, resulting in a high gauge factor ideal for strain sensing. Conversely, perpendicular strain induces pore elongation and maintains inter-fiber connections, stabilizing resistance change and enabling use as a stretchable interconnect. These anisotropic behaviors are maintained under extreme conditions, with no elastomeric support and full metallic coverage. Quantitative analysis of pore aspect ratio dynamics reveals that deformation mode—fiber or pore-driven—is governed by strain direction, explaining the trade-off between sensitivity and mechanical durability. The breathable, elastomer-free design ensures skin compatibility for long-term use, while parylene passivation effectively shields the electrode from ionic interference caused by sweat and biofluids. This work introduces a tunable, dual-functional nanomesh platform optimized for electronic-skin applications, offering a unified solution for both sensing and interconnection demands in wearable electronics.

1. Introduction

Flexible and stretchable electronics have emerged as transformative technologies for next-generation wearable electronic sensors[1,2] healthcare monitoring systems,[3,4] and human–machine interfaces.[5] Among these, skin-conformal electronic systems—commonly referred to as "electronic skins" (e-skins)—are designed to seamlessly interface with the human body by mimicking the mechanical and functional characteristics of natural skin.[6–8] To realize such systems, flexible planar film substrates—polydimethylsiloxane (PDMS),[9,10] Ecoflex[11,12]—have gained increasing attention due to their skin-like modulus and thin structure. These properties result in low flexural rigidity, enabling intimate and conformal contact with curvilinear biological surfaces (Figure S1a, Supporting Information). However, film substrates inherently lack permeability, which can lead to sweat accumulation, discomfort, and histological issues, including allergic or irritant contact dermatitis.[13]

Therefore, nanofiber-based substrates—commonly referred to as nanomeshes—fabricated by electrospinning have been widely studied.[13–31] Owing to their porous structure, these substrates exhibit inherent breathability, which facilitates gas and moisture exchange, thereby suppressing inflammation and enabling continuous health monitoring with minimal discomfort. In our experiments, a 24 h gravimetric water-evaporation assay confirmed vapor permeability of the

H. Cho, G. Yun, J. Jeon, J. Lee, G. Lim
Department of Mechanical Engineering
Pohang University of Science and Technology (POSTECH)
77, Cheongam-ro, Nam-gu, Pohang, Gyeongbuk 37673, Republic of Korea
E-mail: double.arc@postech.ac.kr; limmems@postech.ac.kr

The ORCID identification number(s) for the author(s) of this article can be found under https://doi.org/10.1002/admi.202500600

© 2025 The Author(s). Advanced Materials Interfaces published by Wiley-VCH GmbH. This is an open access article under the terms of the Creative Commons Attribution License, which permits use, distribution and reproduction in any medium, provided the original work is properly cited.

DOI: 10.1002/admi.202500600

P. T. Le, G. Lim
Department of Interdisciplinary Bioscience and Bioengineering
Pohang University of Science and Technology
Pohang 37673, South Korea

T. S. Hwang
Department of Emergency Medicine
Yongin Severance Hospital
Yongin 16995, South Korea

S. W. Kim, J. Lee
Department of Emergency Medicine
College of Medicine
Chungnam National University
266, Munhwa-ro, Jung-gu, Daejoen 35015, Republic of Korea

J. Lee
5 Cellknit Inc.
39, Jigok-ro, Nam-gu, Pohang, Gyeongbuk 37673, Republic of Korea

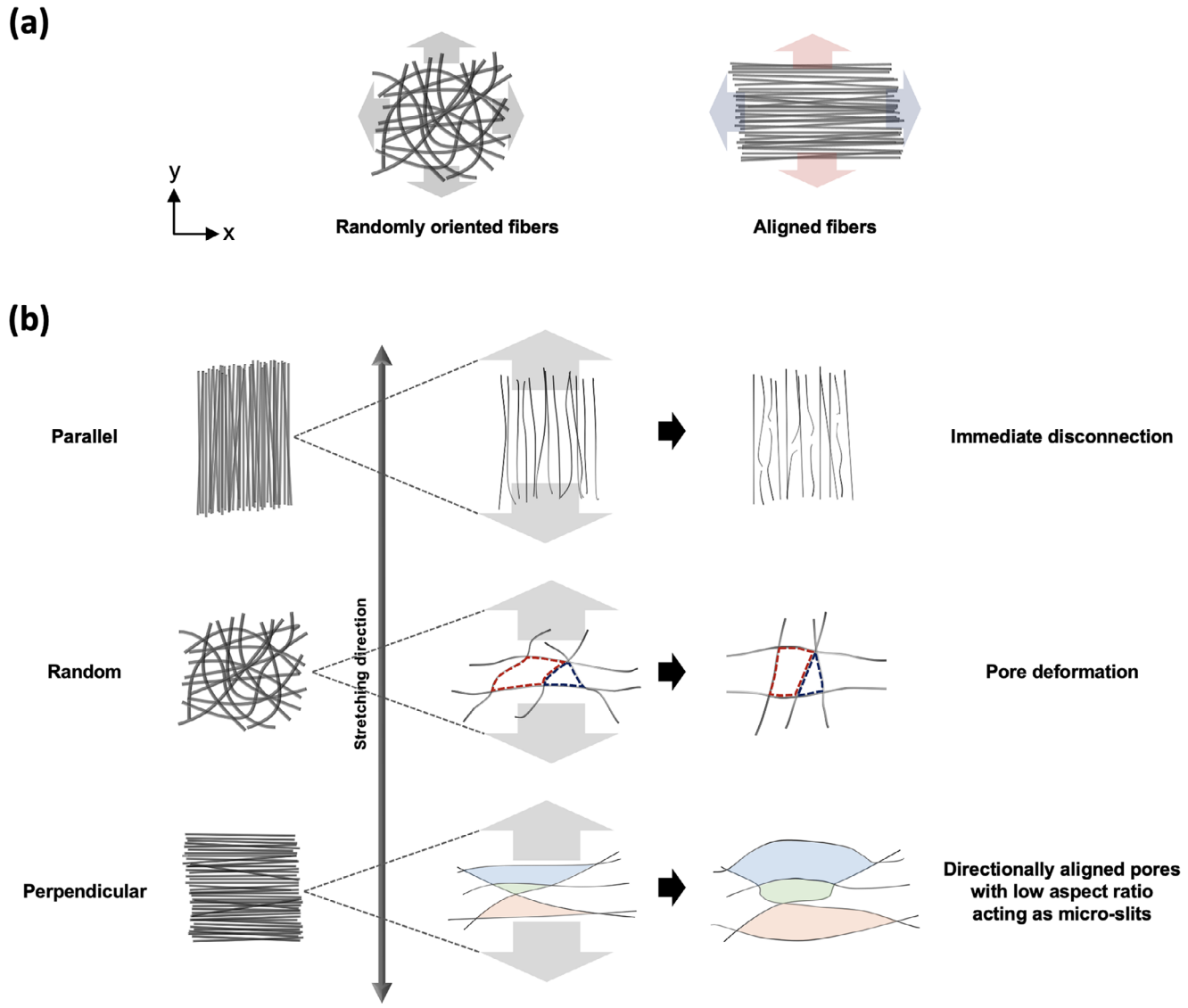

Figure 1. a) Schematic illustration of fiber orientation-dependent mechanical response. Randomly oriented fibers (left) show isotropic deformation under applied strain along both the x- and y-directions, while aligned fibers (right) display anisotropic mechanical responses. b) Schematic representation of deformation mechanisms in nanomeshes with different structures under uniaxial tensile strain.

nanomesh (intermediate mass loss between open and film), and a pig-skin attachment test showed that the nanomesh maintains open sweat ducts whereas films occlude pore openings (Figure S1b,c, Supporting Information). These results highlight the skin compatibility of nanomeshes and their advantage for long-term wearable use. Since nanomeshes are ultrasoft, thin, lightweight, flexible, and breathable, these platforms are particularly attractive for wearable sensing applications. Notably, nanomesh electrodes—comprising electrospun polymer fibers integrated with conductive materials—have demonstrated outstanding performance in signal acquisition, particularly in the detection of: i) physical stress (strain,[18,23] pressure[16]), ii) environmental conditions (temperature,[22] humidity[14,17,20]), and iii) physiological signals (electromyography (EMG),[13,27] electrocardiography (ECG)[28,29]) from the human body.

Despite their promising performance, most nanomesh devices[13–31] still utilize randomly oriented fiber networks, which exhibit mechanically isotropic properties and lack direction-specific tunability. The isotropic nature of conducting networks—arising from randomly oriented nanomesh structures—leads to similar deformation when stretched in either the parallel or the perpendicular direction (**Figure 1a**). This limitation hinders selective response to mechanical deformation along predefined axes—a functionality required for wearable applications operating on synovial joints with direction-dependent strain profiles (e.g., the elbow, knee, and wrist).

To address this limitation, we propose a directionally aligned nanomesh electrode platform fabricated using a rotating drum electrospinning system, which enables controlled fiber orientation. The aligned structure introduces mechanical anisotropy, allowing the electromechanical response of the device to be

© 2025 The Author(s). Advanced Materials Interfaces published by Wiley-VCH GmbH

21967350, 2025, 23, Downloaded from https://advanced.onlinelibrary.wiley.com/doi/10.1002/admi.202500600 by Yonsei University Med Library, Wiley Online Library on [13/01/2026]. See the Terms and Conditions (https://onlinelibrary.wiley.com/terms-and-conditions) on Wiley Online Library for rules of use; OA articles are governed by the applicable Creative Commons License

21967350, 2025, 23, Downloaded from https://advanced.onlinelibrary.wiley.com/doi/10.1002/admi.202500600 by Yonsei University Med Library, Wiley Online Library on [13/01/2026]. See the Terms and Conditions (https://onlinelibrary.wiley.com/terms-and-conditions) on Wiley Online Library for rules of use; OA articles are governed by the applicable Creative Commons License

tailored according to fiber alignment direction (Figure 1a). Importantly, we show that directional fiber alignment—either parallel or perpendicular to the strain axis—enables two distinct operating regimes that stem from different deformation mechanisms (schematically summarized in Figure 1b):

1) When fibers are aligned parallel to the direction of strain, the applied tension is directly transferred to the fibers, causing immediate elongation. This tensile strain deforms and eventually fractures the gold layer coated on the fiber surface, leading to a pronounced increase in resistance. In addition, the parallel alignment exhibits the lowest resistance among all structures, as enhanced charge transport significantly improves their performance as electrical channels.[32,33] These behaviors enable the structure to function as a high-sensitivity strain sensor.[34–36]
2) When fibers are aligned perpendicular to the strain direction, the applied tension increases the gap between fibers while preserving existing node-to-node connections, thereby allowing the network to deform structurally before significant stress is applied to individual fibers. Similarly, the perpendicular conductive network remains intact, and the overall resistance shows minimal change,[35,36] with comparable stretchability,[37–39] making its structure suitable for stable electrical interconnects.

Ensuring environmental robustness is equally important for practical e-skin operation. In solution-based processes,[26–30] silver nanowires (AgNWs) are distributed across nanomesh substrates, with the nanowires directly interfacing with the external environment; however, AgNWs are highly susceptible to chemical degradation under sweat or humidity.[40] In our vacuum-based approach,[13–20] gold (Au), a chemically inert and biocompatible material,[41] is thermally evaporated to form the electrode layer and subsequently encapsulated with a thin parylene coating. The hydrophobic parylene layer (static water contact angle 107.6°) provides water protection (Figure S2a, Supporting Information) and suppresses ionic penetration, as verified by copper (Cu) control experiments: bare Cu electrodes corroded and exhibited sharp impedance drift in phosphate-buffered saline (PBS), whereas parylene-passivated Cu remained visually intact and electrically stable over time (Figure S2b,c, Supporting Information). The active electrode area was then selectively defined using oxygen reactive ion etching (RIE) to minimize environmental exposure.

Previous reports on alignment-induced anisotropy have mainly targeted tunable strain sensing or interconnect applications, yet these systems often relied on elastomer films or dense composite substrates that lacked breathability and were not designed for ionic passivation. In contrast, this work provides the first proof-of-concept demonstration of electromechanical anisotropy in a breathable, parylene-passivated nanomesh electrode, combining orientation-dependent dual functionality with verified breathability, skin compatibility, and environmental robustness.

Building on this prior work,[42–45] we investigate how the deformation mechanisms change depending on fiber orientation within a nanomesh substrate platform. Furthermore, we analyze the evolution of pore geometry under mechanical strain by quantifying the anisotropy of the pore aspect ratio (height/width) across different alignment conditions. Our findings indicate that stretchability is significantly influenced by the mode of strain accommodation—either through pore-level deformation or by fiber-level elongation. Specifically, pores in perpendicularly aligned meshes initially exhibit low aspect ratios and elongate preferentially along the strain axis under uniaxial tensile strain, thereby increasing anisotropy and allowing greater mechanical compliance. In contrast, in parallel-aligned meshes, the strain acts directly on the fibers, which rupture after only minimal deformation. This correlation highlights pore-level structural behavior as a key mechanism underlying the observed electromechanical performance. We believe this approach provides a foundational strategy for building multifunctional wearable systems, where individual elements can be engineered within a single material platform featuring geometrically tunable behavior to function either as strain sensors or as reliable interconnects.

2. Results and Discussion

2.1. Fabrication and Characterization of Nanomesh Electrodes

Nanomesh electrodes were fabricated by electrospinning polyurethane (PU) nanofibers, followed by sequential parylene coating, Au evaporation, and O_2 plasma etching (**Figure 2a**). PU was chosen for its elastomeric properties and biocompatibility, making it suitable for wearable devices.[46] Using a stationary plate or a rotating drum collector (Figure S3, Supporting Information), we prepared randomly oriented, parallel-aligned, and perpendicularly aligned nanomeshes. After electrospinning, biocompatible parylene was deposited by chemical vapor deposition[54] to reinforce the fibrous scaffold and provide encapsulation, and gold (Au) was subsequently deposited via thermal evaporation to form the conductive layer. Finally, oxygen RIE (30 sccm, 50 W) was used to selectively remove parylene and expose the active electrode area.

Optical microscope and scanning electron microscopy (SEM) observations confirmed the formation of uniform nanomesh structures (Figure 2b–d). Without parylene, the meshes collapsed upon removal of the polyethylene terephthalate (PET) transfer window, whereas parylene-coated meshes retained a stable free-standing form (Figure 2c). This result highlights the critical role of parylene in structural stabilization. Furthermore, parylene suppressed resistance fluctuations under ambient conditions (Figure 2e), improving long-term electrical reliability. SEM–EDS mapping and spectra demonstrated uniform Au deposition and strong Au peaks along PU fibers, verifying successful metallization (Figure S4, Supporting Information).

The passivation role of parylene was further supported by control tests. After oxygen RIE, the active electrode areas were clearly defined (Figure S5, Supporting Information), ensuring that only the necessary regions were exposed. Cross-sectional SEM revealed that the overall electrode thickness was ≈2.4 μm, including both the nanofiber scaffold (≈1.8–2.2 μm) and the parylene/Au layers (≈200 nm) (Figure S6, Supporting Information).

Electrospinning collection time strongly influenced the mechanical properties of the nanomeshes. As collection time increased from 10 to 90 s, fiber density and coverage increased,

 © 2025 The Author(s). Advanced Materials Interfaces published by Wiley-VCH GmbH

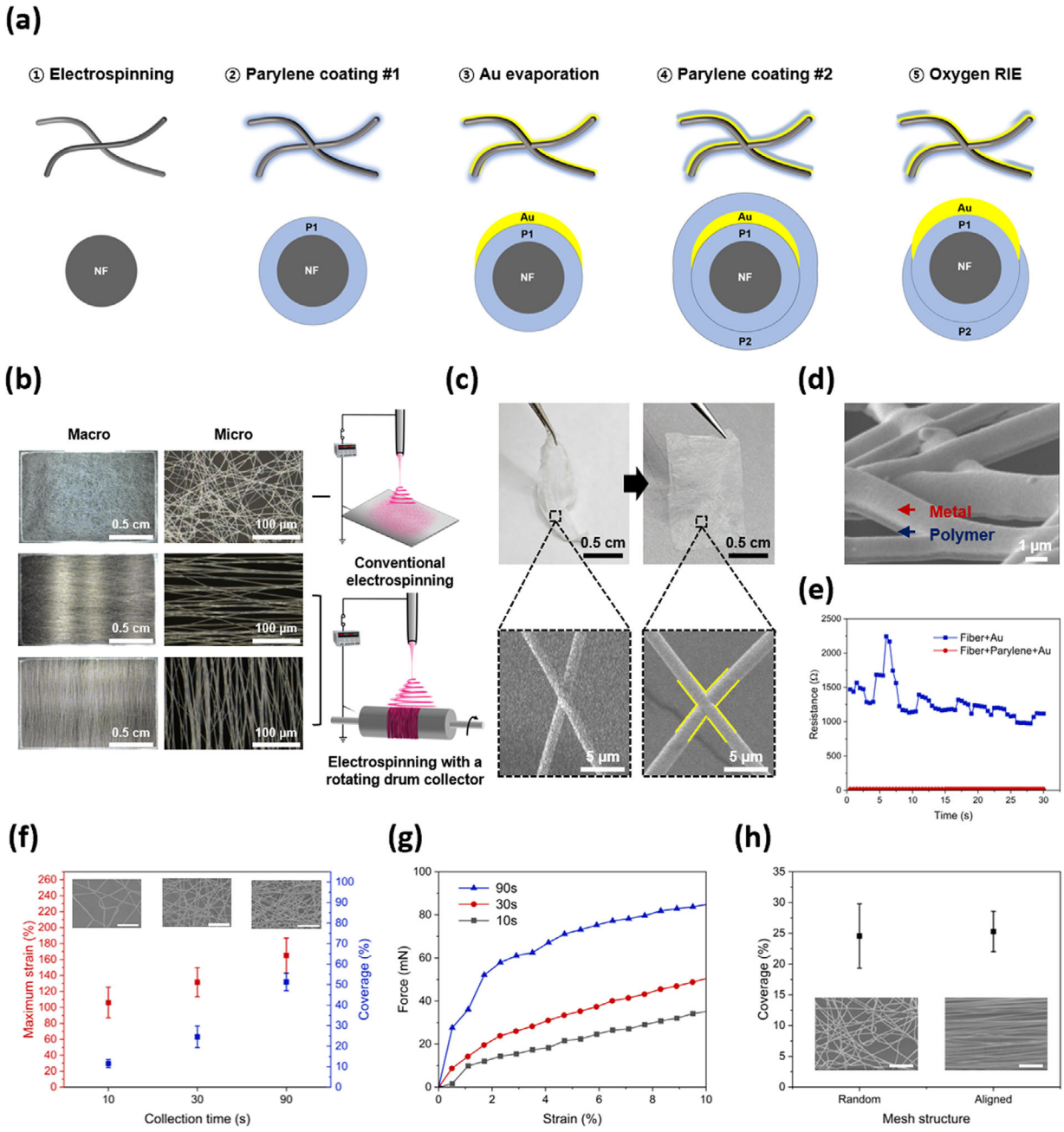

Figure 2. Fabrication and characterization of nanomesh electrodes. a) Schematic illustration of the fabrication process. b) Optical microscope images of the polyurethane nanomesh at macro- and microscale, showing randomly oriented (top), parallel-aligned (middle), and perpendicularly aligned (bottom) nanofibers. c) Side-by-side comparison of nanomeshes without (left) and with parylene coating (right) after removal of the PET window, highlighting the essential role of parylene in forming a stable free-standing substrate. d) SEM image of a nanomesh electrode after Au evaporation. e) Resistance changes over time, highlighting the role of parylene coating in suppressing fluctuations and stabilizing electrical conduction. f) Stretchability and fiber coverage of nanomeshes fabricated with different electrospinning collection times ($N = 15$). Scale bar, 50 μm. g) Softness of nanomeshes fabricated with different electrospinning collection times. h) Comparison of nanofiber coverage between randomly oriented and aligned nanomeshes ($N = 25$). Scale bar, 50 μm.

leading to higher stretchability but reduced softness due to greater inter-fiber junctions and stacking.[47] These trends are summarized in stretchability and softness plots (Figure 2f,g). Based on these results, a collection time of 30 s was selected to produce monolayer meshes with ≈24.7% coverage, providing sufficient structural stability while enabling clear evaluation of anisotropic effects.

The extent and distribution of Au coverage also had a major impact on mechanical performance. When the entire mesh was coated with Au, the brittle metallic layer dominated the

© 2025 The Author(s). Advanced Materials Interfaces published by Wiley-VCH GmbH

21967350, 2025, 23, Downloaded from https://advanced.onlinelibrary.wiley.com/doi/10.1002/admi.202500600 by Yonsei University Med Library, Wiley Online Library on [13/01/2026]. See the Terms and Conditions (https://onlinelibrary.wiley.com/terms-and-conditions) on Wiley Online Library for rules of use; OA articles are governed by the applicable Creative Commons License

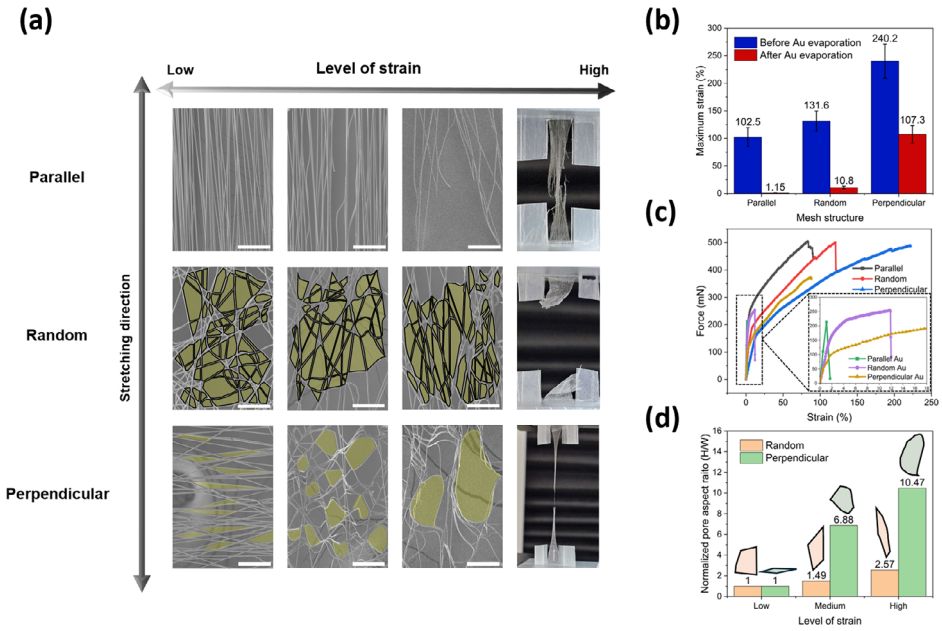

Figure 3. Mechanical properties of nanomeshes under uniaxial tensile strain. a) Structural deformation of nanomeshes with parallel-aligned, randomly oriented, and perpendicularly aligned fibers under increasing strain levels (low, medium, and high represent qualitative deformation stages—from intact to fracture—for each mesh type. Scale bar, 50 µm. Parallel-aligned meshes deform mainly through fiber elongation and direct stress concentration, whereas perpendicular-aligned meshes deform through pore elongation accompanied by gradual fiber rotation and variation of junction contact area, leading to efficient stress redistribution. Random meshes show mixed deformation responses. b) Effect of Au evaporation on the stretchability of nanomeshes with different mesh structures ($N = 15$). c) Corresponding force-strain curves. The strain levels of these stages differ among structures, but correspond directly to the strain morphology in panel (a). d) Normalized changes in pore aspect ratio (height/width) under varying strain levels (low, medium, high) for nanomeshes with randomly oriented and perpendicularly aligned fibers.

deformation behavior, resulting in early cracking and electrical failure. In contrast, shadow-mask patterning restricted Au deposition to local electrode regions (≈35% coverage), reducing unnecessary stiffening while preserving continuous conduction within the electrodes (Figure S7, Supporting Information). SEM observations under tensile strain confirmed that the underlying PU fibers remained continuous, while the Au coating fractured and separated (Figure S8, Supporting Information). This mechanical mismatch explains why the pristine polymer network tolerated strains >100%, whereas Au-coated meshes lost electrical continuity at ≈10% strain.

Finally, structure-dependent mechanics were further analyzed. To fairly assess anisotropy arising from mesh structure, fiber coverage was quantified by threshold-based ImageJ analysis and adjusted to comparable levels for both randomly oriented and aligned meshes (Figure 2h). Force–strain curves of meshes with and without Au deposition showed marked reductions in stretchability after metallization, particularly in the parallel configuration (Figure S9, Supporting Information). Directional analysis with ImageJ confirmed the anisotropic alignment of electrospun fibers (Figure S10, Supporting Information), establishing a baseline for the electromechanical anisotropy investigated in the following sections.

2.2. Mechanical Properties

To compare the anisotropy of aligned meshes with conventional random orientation, three types of nanomeshes—parallel-aligned, randomly oriented, and perpendicularly aligned—were subjected to uniaxial tensile strain (**Figure 3a**). Unlike previous studies on anisotropy, here the nanomesh itself, reinforced with parylene, served as the stretchable substrate. Free-standing aligned substrates have rarely been reported. Since perfect alignment is difficult to achieve—even at high drum speeds, where air turbulence induces partial misalignment—paradoxically, such misalignment promotes the formation of fiber–fiber junctions, thereby enabling the fabrication of free-standing substrates even in aligned structures.[48] A directionality analysis using Fourier components in ImageJ confirmed that ≈64% of fibers were aligned near 2.7° with a dispersion of 9.3°, resulting in predominant alignment but also sufficient inter-fiber contact points to allow a mechanically stable free-standing mesh (Figure S10, Supporting Information).

Distinct deformation mechanisms were observed depending on fiber orientation. Parallel-aligned meshes deformed primarily at the fiber level, where axial stress concentrated along continuous fibers, leading to early fracture once their tensile limit was exceeded. In contrast, randomly oriented and perpendicularly aligned meshes exhibited pore-level deformation, with pores elongating to dissipate stress before it transferred to the fibers. As shown in Figure 3b,c, the stretchability of the parallel, random, and perpendicular meshes reached ≈102.5%, 131.6%, and 240.2%, respectively. SEM observations during stretching (Figure S11, Supporting Information) confirmed these two regimes: fiber elongation and fracture in parallel meshes versus progressive pore opening and fiber rotation in perpendicular meshes.

© 2025 The Author(s). Advanced Materials Interfaces published by Wiley-VCH GmbH

21967350, 2025, 23, Downloaded from https://advanced.onlinelibrary.wiley.com/doi/10.1002/admi.202500600 by Yonsei University Med Library, Wiley Online Library on [13/01/2026]. See the Terms and Conditions (https://onlinelibrary.wiley.com/terms-and-conditions) on Wiley Online Library for rules of use; OA articles are governed by the applicable Creative Commons License

Quantitative analysis of pore aspect ratio further distinguished random and perpendicular structures (Figure 3d). In random meshes, initial pore shapes varied widely, and pores elongated until high aspect ratios limited further deformation, forcing a transition to fiber-level strain. In contrast, perpendicular meshes had uniformly low initial aspect ratios aligned with the strain axis, enabling coherent pore elongation and much greater overall stretchability (aspect ratio increase: random 257%, perpendicular 1047%). This mechanistic difference explains why random meshes display mixed, heterogeneous deformation while perpendicular meshes deform uniformly.

These pathways also clarify the trade-off between sensitivity and durability. Parallel meshes, dominated by fiber-level deformation, respond with high sensitivity but fail at small strains. Perpendicular meshes, dominated by pore elongation and fiber rotation, maintain conduction across large strains but exhibit low sensitivity. Random meshes fall between these extremes.

After Au deposition, the same trends persisted but with reduced compliance due to the mechanical mismatch between the brittle Au layer and the soft PU network. As shown in Figure 3b, stretchability decreased dramatically: parallel meshes fractured electrically at ≈1.15%, random at 10.8%, while perpendicular meshes still reached ≈107.3%. In parallel meshes, direct stress transfer caused the Au to rupture immediately, yielding ultrahigh gauge factors but a limited working range. In random meshes, pore deformation could not compensate for the brittleness of Au, leading to sharp failure. By contrast, perpendicular meshes benefited from low-aspect-ratio pores that initially elongated and rotated like micro-slits (similar to kirigami patterns[49]), dissipating applied stress. At higher strains, cracks appeared in the Au layer, but conduction was preserved as the underlying PU fibers continued to stretch (Figure S11, Supporting Information). Only at extreme deformation did the PU network itself fracture, confirming that perpendicular alignment provides a stepwise mechanism of stress release that maintains conductivity over a wide range.

Finally, strategies to expand the working range of parallel meshes were explored. By introducing multiple parallel slits[50] into aligned nanomesh membranes, the effective stretchability in the parallel direction increased significantly, while parylene encapsulation preserved structural stability through junction-free reinforcement. As shown in Figure S12 (Supporting Information), slit-engineered meshes extended the maximum strain without compromising integrity, demonstrating a practical design pathway to overcome the intrinsic fragility of fiber-level deformation.

2.3. Electrical Properties

To function effectively as electrodes, electrical continuity must be preserved during deformation. We evaluated the relative resistance change ($\Delta R/R_0$, where R_0 is the initial resistance and ΔR the resistance change under strain) of the three nanomesh structures (**Figure 4a**). In all cases, resistance increased with strain, reflecting the progressive reduction of conductive pathways. Two sequential phenomena were observed (Figure S11): an initial regime dominated by pore-level deformation, followed by fiber-level deformation that ultimately led to the disconnection of the Au layer and then of the fibers. At this stage, all structures reached open circuit, though the strain thresholds differed by orientation.

In the pristine state, the parallel-aligned nanomesh exhibited the lowest initial resistance (9.34 Ω, Figure 4b) due to highly connected conductive paths along aligned fibers. However, tensile stress was directly transferred to these fibers, causing immediate rupture of the Au layer. This resulted in discontinuities and a very steep resistance response, producing an exceptionally high gauge factor (GF = 5325 at 1% strain, Figure 4c). Such behavior highlights the potential of parallel meshes for high-sensitivity strain sensing, though their working range is limited.

By contrast, the perpendicular-aligned mesh provided the highest initial resistance (98.7 Ω, Figure 4b) because electron transport followed longer, tortuous paths. Upon stretching, pores elongated and redistributed stress while preserving inter-fiber contacts, resulting in minimal resistance changes over large strains. This yielded a very low GF of 0.17 in the 0–50% strain range (Figure 4c). The random mesh showed intermediate properties (GF = 6.68 at 0–10% strain). Although other strain sensors have reported ultrahigh gauge factors (10^3–10^5),[51,52] our objective is not to maximize sensitivity but to highlight anisotropy as the design principle. Parallel meshes deliver high sensitivity at small strains, while perpendicular meshes maintain stable conduction over broad strain ranges, a dual functionality absent in previous isotropic nanomesh electrodes.

To evaluate durability, cyclic tests were performed on perpendicular meshes at 25% and 50% strain (Figure 4d). Relative resistance increased slightly during stretching (1.31% at 25% strain; 4.14% at 50% strain) but recovered upon release, returning near the initial state (0.58% and 2.91%, respectively). SEM imaging confirmed that although minor fiber or Au disconnections appeared at high strain, overall morphology remained intact, with pores elongating and closing reversibly (Figure 4e). This stress dissipation, resembling a kirigami-like micro-slit mechanism, explains the ability of perpendicular meshes to sustain wide strain ranges with minimal overshoot and stable conduction.

Taken together, these results demonstrate the intrinsic anisotropy of aligned nanomesh electrodes: parallel meshes offer high sensitivity, while perpendicular meshes ensure robustness and low drift under repeated deformation. Combined with breathability, ionic passivation, and skin compatibility shown earlier, this anisotropy-enabled dual functionality provides a versatile foundation for e-skin applications.

2.4. On-Skin Application

The anisotropic properties of nanomesh electrodes—particularly the high stretchability and low gauge factor of perpendicularly aligned structures—make them promising candidates for use as interconnects in wearable systems. To evaluate this potential, nanomeshes with either random or perpendicular fiber orientations were attached to the wrist and subjected to flexion-extension motion (**Figure 5a,b**). For secure conformal attachment, a thin polyvinylpyrrolidone (PVP) fiber mat was first electrospun onto the skin; upon contact with water vapor, it dissolved to form a transient adhesive layer. The nanomesh electrode was then laminated onto the skin and connected to an external circuit.

© 2025 The Author(s). Advanced Materials Interfaces published by Wiley-VCH GmbH

21967350, 2025, 23, Downloaded from https://advanced.onlinelibrary.wiley.com/doi/10.1002/admi.202500600 by Yonsei University Med Library, Wiley Online Library on [13/01/2026]. See the Terms and Conditions (https://onlinelibrary.wiley.com/terms-and-conditions) on Wiley Online Library for rules of use; OA articles are governed by the applicable Creative Commons License

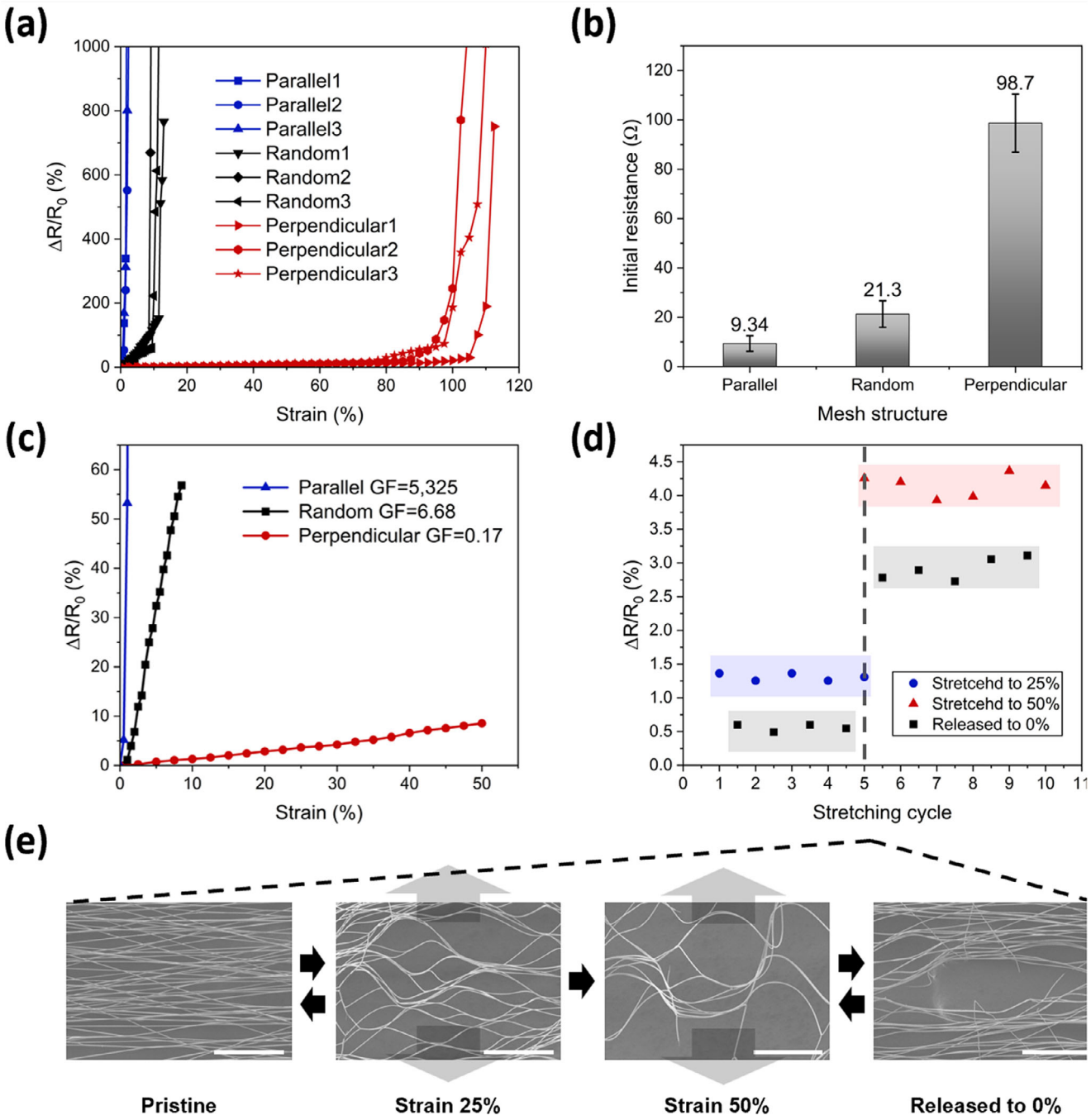

Figure 4. Electrical performances of nanomesh electrodes. a) Relative resistance changes of nanomeshes with different structures under uniaxial tensile strain. b) Initial resistance (N = 15). c) Gauge factors of nanomeshes measured within the strain ranges corresponding to parallel-aligned (0–1%), random oriented (0–10%), and perpendicular-aligned (0–50%) fibers. d) Cyclic stretching and releasing at 25% and 50% strain, respectively. e) SEM images of nanomeshes in the pristine state, at 25% and 50% strain, and after release to 0%. Scale bar, 100 μm.

During wrist flexion, the perpendicularly aligned nanomesh maintained electrical continuity, whereas the randomly oriented nanomesh failed and exhibited an open circuit (Figure 5c). This result highlights the unique role of anisotropic pore structures: in perpendicular meshes, low-aspect-ratio pores aligned along the strain axis dissipate tensile stress in a kirigami-like fashion, preserving conduction paths even under complex joint motion. By contrast, random meshes deform heterogeneously and cannot sustain connectivity under large displacements. These findings confirm that fiber orientation is a decisive factor in enabling robust interconnect behavior, even when conventional metallic coatings such as Au inherently lack stretchability.[53]

Beyond simple wrist flexion, we also investigated dynamic stability under repeated on-skin deformation. Perpendicular

© 2025 The Author(s). Advanced Materials Interfaces published by Wiley-VCH GmbH

21967350, 2025, 23, Downloaded from https://advanced.onlinelibrary.wiley.com/doi/10.1002/admi.202500600 by Yonsei University Med Library, Wiley Online Library on [13/01/2026]. See the Terms and Conditions (https://onlinelibrary.wiley.com/terms-and-conditions) on Wiley Online Library for rules of use; OA articles are governed by the applicable Creative Commons License

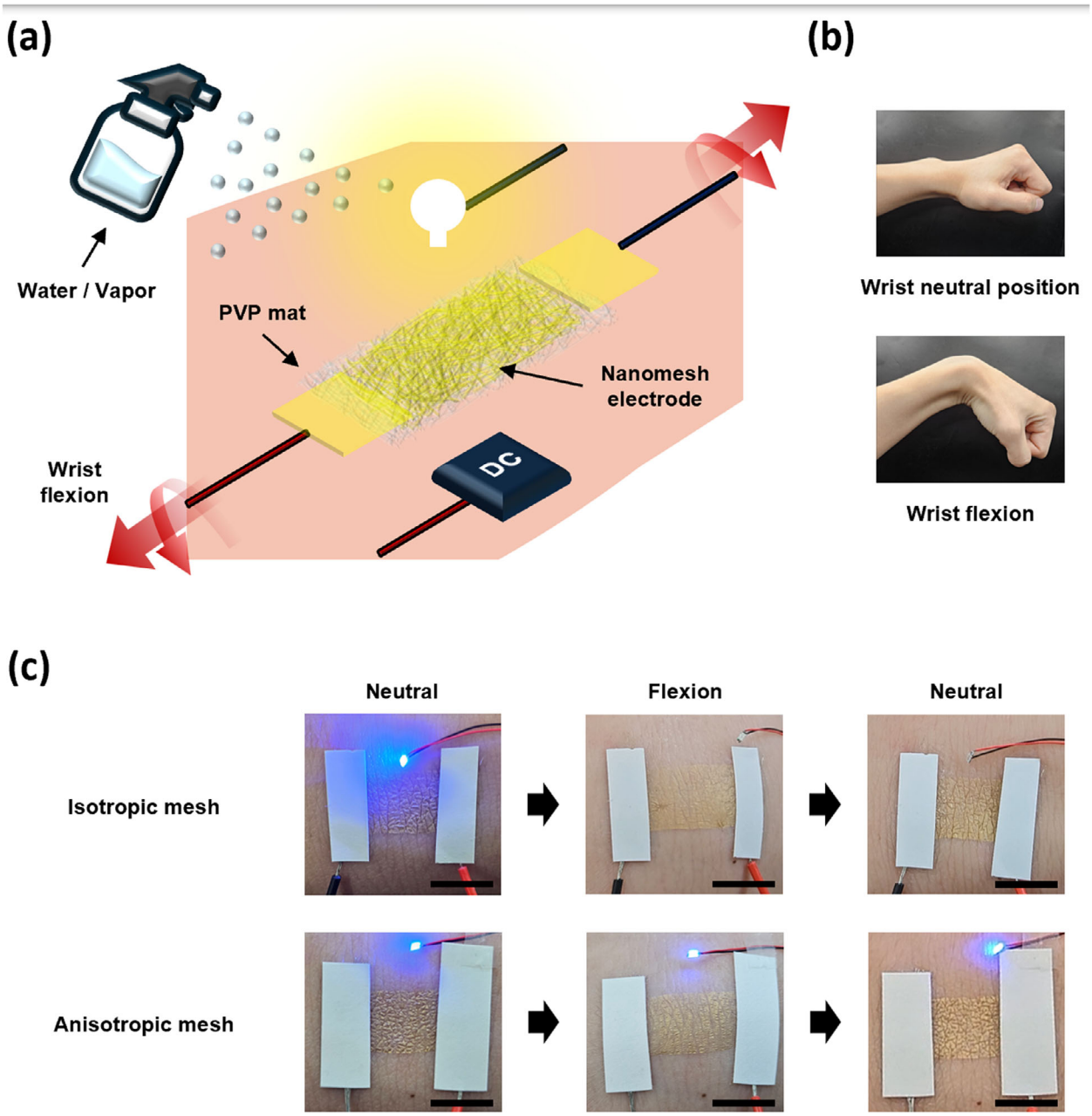

Figure 5. On-skin application. a) Schematic illustration of the nanomesh electrode during wrist flexion. b) Wrist flexion. c) Conductivity retention of the nanomesh electrode during wrist flexion. Scale bar, 1 cm.

nanomesh electrodes attached to the skin were subjected to >1000 manual stretching and compression cycles. As shown in Figure S13 (Supporting Information), resistance remained nearly constant throughout the test, demonstrating negligible drift and confirming long-term reliability under repeated mechanical loading.

The platform is also compatible with scalable fabrication. Large-area nanomesh sheets with patterned electrode regions were uniformly produced over centimeter-scale substrates (Figure S14a, Supporting Information), and roll-to-roll electrospinning enabled continuous preparation of aligned nanomeshes (Figure S14b, Supporting Information). These results establish the feasibility of mass manufacturing and integration into practical wearable devices.

Finally, orientation programmability allows simple device-level integration. Two aligned nanomesh electrodes were patterned and stacked orthogonally to form a parallel-plate capacitor configuration (Figure S15, Supporting Information). This proof-of-concept demonstration illustrates how orientation control can be exploited to construct multifunctional devices without complex processing steps.

© 2025 The Author(s). Advanced Materials Interfaces published by Wiley-VCH GmbH

21967350, 2025, 23, Downloaded from https://advanced.onlinelibrary.wiley.com/doi/10.1002/admi.202500600 by Yonsei University Med Library, Wiley Online Library on [13/01/2026]. See the Terms and Conditions (https://onlinelibrary.wiley.com/terms-and-conditions) on Wiley Online Library for rules of use; OA articles are governed by the applicable Creative Commons License

Taken together, these results highlight the potential of aligned nanomesh electrodes for skin-integrated electronics: perpendicular meshes function as stable interconnects during joint motion, exhibit robust cyclic stability, can be manufactured at scale, and can be combined in orthogonal configurations for device integration.

3. Conclusion

In this work, we demonstrated a fiber-alignment strategy to induce electromechanical anisotropy in free-standing nanomesh electrodes. By controlling the orientation of electrospun fibers, a single material platform can function either as a high-sensitivity strain sensor (parallel alignment) or a stretchable interconnect (perpendicular alignment), with performance determined solely by strain direction. This anisotropy is particularly advantageous for skin-mounted applications, such as joints where deformation is inherently directional. Even under extreme conditions—monolayer, elastomer-free substrates with full metallic coverage—the devices preserved their characteristic responses: parallel meshes produced ultrahigh gauge factors, while perpendicular meshes maintained conductivity over wide strain ranges. Quantitative pore-aspect-ratio analysis confirmed that these behaviors arise from distinct deformation mechanisms: fiber-level elongation versus pore-level expansion.

Equally important, the nanomesh design integrates breathability, skin compatibility, and ionic passivation, enabling robust physiological interfacing. Breathability was validated by gravimetric water-evaporation assays and pig-skin attachment tests, which confirmed vapor transport and preserved sweat ducts, unlike commercial films that occluded pores. Ionic passivation was demonstrated using Cu control electrodes: bare Cu corroded and showed impedance drift in PBS, whereas parylene-passivated Cu remained stable. These results verify that the platform resists both moisture accumulation and ionic interference, ensuring long-term comfort and stability during wear.

Dynamic stability was further confirmed through > 1000 cycles of on-skin deformation (stretching, compression, twisting), with negligible resistance drift, and large-area sheets were produced using roll-to-roll electrospinning, demonstrating scalable fabrication. Moreover, orthogonal stacking of aligned meshes enabled a simple capacitor configuration, highlighting the feasibility of orientation-based device integration beyond strain sensing or interconnect applications.

Together, these results establish a structurally and physiologically compatible electrode platform with directional tunability, multifunctionality, and environmental robustness, providing a promising foundation for next-generation wearable and skin-interfaced electronic systems. While not exhaustive of all possible use cases, this work demonstrates a proof-of-concept approach that unifies anisotropy, breathability, and passivation within a versatile nanomesh architecture, adaptable across diverse wearable technologies.

4. Experimental Section

Materials: A thermoplastic polyurethane elastomer (PU) (Pellethane 2363-80AE, Lubrizol) was used as the base polymer for electrospinning. Di-chloro-di-p-xylylene (diX C) (Daisan Kasei) was used as the dimer precursor for the chemical vapor deposition (CVD) (OBT-PC300, Obang Technology) of Parylene C. Gold (Au) was deposited via physical vapor deposition (PVD) (The1-MTE1, The One Science) using 99.999% pure gold targets. For the adhesive layer, polyvinylpyrrolidone (PVP) (Sigma–Aldrich) was electrospun. All solvents, including N,N-dimethylformamide (DMF), tetrahydrofuran (THF), and ethanol were analytical grade and used as received.

Electrospinning: PU pellet was dissolved in a mixed solvent (DMF: THF with a volume ratio of 6:4) to prepare the precursor solution of 10 weight percent (wt.%). Electrospun nanofiber meshes were fabricated by using two types of collectors to control fiber alignment. For aligned meshes, a rotating drum collector (diameter: 10 cm; rotational speed: 500 rpm) was used to induce uniaxial fiber alignment. In contrast, randomly oriented meshes were obtained by collecting fibers on a stationary flat metal plate. For easy delamination of the nanomesh sheet, silicone-coated paper was placed on the metal collector. A 10 wt.% PU solution was electrospun at 10 kV with a 1 mL h^{-1} flow rate and 10 cm tip-to-collector distance. The electrospinning time was set to 10 min for aligned fibers and 30 s for randomly oriented fibers to collect approximately the same amount of electrospun fibers. The resulting meshes were dried under vacuum overnight to remove residual solvent. The electrospun PU fiber sheet was transferred to a transparent PET film used as a temporary supporting window with dimensions of 15 × 10 mm^2. Samples were categorized as randomly oriented, parallel-aligned, and perpendicularly aligned. Parallel and perpendicular alignments were defined based on the angle between the fiber axis and the direction of the transfer window, which was adjusted manually during the transfer process.

Sample Preparation: Samples were prepared according to the specific experimental requirements. For uniaxial tensile testing, two types of samples were prepared: one with PU fibers coated with 200 nm of parylene, and the other with PU fibers coated with 200 nm of parylene and 100 nm of Au. Au was uniformly evaporated across the entire nanomesh surface to ensure complete coverage. For real-world applications, a shadow mask was used for selective Au evaporatation, followed by an additional 200 nm thick parylene coating to encapsulate the electrode layer. Oxygen plasma reactive ion etching (RIE) (CIONE 4, Femto Science) was then used to selectively remove parylene from the active electrode areas, while preserving the encapsulation in the interconnect regions. However, for the on-skin application specific to this study, no shadow mask was used for Au evaporation.

Structural Characterization: Scanning electron microscopy (SEM) (SNE-4500 M, SEC) and optical microscope (BX53M, OLYMPUS) was used to examine the structural features of the nanomesh, including fiber morphology, pore geometry, and deformation behaviors under uniaxial tensile strain. To enable a fair comparison of mesh structures independent of fiber density, fiber coverage (%) was quantified using threshold-based analysis in ImageJ. Fiber orientation was also evaluated by using directional analysis with ImageJ.

Mechanical Testing: Samples (length: 15 mm; width: 10 mm) were stretched with a universal testing machine (34SC-1, Instron) at the speed of 180 μm s^{-1} until failure. A slit was introduced along the side of the OHP film to facilitate the stretching of the mesh, while the top and bottom portions of the OHP film, in the direction of stretching, were securely clamped at both ends during the testing.

Electrical Measurements: To investigate electrical continuity, the relative resistance change of each mesh structure was continuously monitored during uniaxial stretching. An anisotropic conductive tape (9703, 3 M) was attached to the OHP film on the clamped sides, along the direction of stretching, to secure the Cu wiring to a digital multimeter (15B+, Fluke). In addition, a simple cyclic stretching test was performed on the perpendicularly aligned nanomesh samples. The samples were subjected to five cycles of loading and releasing at 25% and 50% strain, respectively.

On-Skin Application: To demonstrate conformal contact of the nanomesh electrodes on human skin, electrodes were laminated onto the wrist following the transfer of electrospun PVP fiber mats. A 12 wt.% PVP precursor solution was prepared by dissolving PVP powder in a 7:3 mixture of ethanol and deionized (DI) water. The solution was electrospun at 12 kV

© 2025 The Author(s). Advanced Materials Interfaces published by Wiley-VCH GmbH

21967350, 2025, 23, Downloaded from https://advanced.onlinelibrary.wiley.com/doi/10.1002/admi.202500600 by Yonsei University Med Library, Wiley Online Library on [13/01/2026]. See the Terms and Conditions (https://onlinelibrary.wiley.com/terms-and-conditions) on Wiley Online Library for rules of use; OA articles are governed by the applicable Creative Commons License

with a flow rate of 1.0 mL h^{-1} and a tip-to-collector distance of 10 cm. The fiber mats were applied to the skin and sprayed with water or vapor, allowing the PVP to dissolve and form a thin adhesive layer that bonded the nanomesh electrodes to the skin. Two types of nanomesh electrodes were tested: i) a conventional randomly oriented mesh and ii) a perpendicularly aligned mesh. To visualize electrical performance under wrist flexion, a micro-LED was connected to the Cu wiring with anisotropic conductive tape on the electrode, and its illumination during flexion qualitatively confirmed electrical conductance.

Water-Evaporation Assay: Glass vials (10 g initial water) covered with open, nanomesh, or parylene-film lids; mass recorded at set intervals up to 24 h at room-temperature.

Cu-Electrode PBS Test: Copper (Cu) was evaporated instead; half encapsulated with parylene, while the other half remained bare; samples immersed in phosphate-buffered saline (PBS) at room-temperature; impedance measured periodically; photographs taken to document visual changes.

Supporting Information

Supporting Information is available from the Wiley Online Library or from the author.

Acknowledgements

This research was supported by Basic Science Research Program through the National Research Foundation of Korea (NRF) funded by the Ministry of Education (RS-2024-00452785)., by a faculty research grant of Yonsei University College of Medicine (6-2023-0087), and by Cellknit Inc. H.C. designed and performed all experiments. H.C., G.Y., P.T.L., T.S.H., J.J., S.W.K., and J.L. investigated data. J.L. conceived and designed the idea and financially supported. G.L. supervised this manuscript.

Conflict of Interest

Jungho Lee is the founder and CEO of Cellknit Inc., which holds the commercialization rights to the technology described in this study. The other authors declare no conflict of interest.

Data Availability Statement

The data that support the findings of this study are available in the supplementary material of this article.

Keywords

breathability, electromechanical anisotropy, electronic skins, fiber alignment, interconnects, nanomesh electrodes, strain sensors

Received: June 30, 2025
Revised: September 5, 2025
Published online: October 21, 2025

[1] M. Amjadi, K. U. Kyung, I. Park, M. Sitti, *Adv. Funct. Mater.* *26*, 1678.
[2] W. Gao, H. Ota, D. Kiriya, K. Takei, A. Javey, *Acc. Chem. Res.* **2019**, *52*, 523.
[3] J. Kim, A. S. Campbell, B. E.-F. de Ávila, J. Wang, *Nat. Biotechnol.* **2019**, *37*, 389.
[4] S. Gong, Y. Lu, J. Yin, A. Levin, W. Cheng, *Chem. Rev.* **2024**, *124*, 455.
[5] W. Heng, S. Solomon, W. Gao, *Adv. Mater.* **2022**, *34*, 2107902.
[6] T. Someya, T. Sekitani, S. Iba, Y. Kato, H. Kawaguchi, T. Sakurai, *Proc. Natl. Acad. Sci.* **2004**, *101*, 9966.
[7] D. H. Kim, N. Lu, R. Ma, Y. S. Kim, R. H. Kim, S. Wang, J. Wu, S. M. Won, H.u Tao, A. Islam, K.i J. Yu, T.-I. Kim, R. Chowdhury, M. Ying, L. Xu, M. Li, H. J. Chung, H. Keum, M. McCormick, P. Liu, Y. W. Zhang, F. G. Omenetto, Y. Huang, T. Coleman, J. A. Rogers, *Science* **2011**, *333*, 838.
[8] Z. Yuan, G. Shen, *Mater. Today* **2023**, *64*, 165.
[9] J. W. Jeong, W. H. Yeo, A. Akhtar, J. J. Norton, Y. J. Kwack, S. Li, S. Y. Jung, Y. Su, W. Lee, J. Xia, *Adv. Mater.* **2013**, *25*, 6839.
[10] Z. Liu, D. Qi, P. Guo, Y. Liu, B. Zhu, H. Yang, Y. Liu, B. Li, C. Zhang, J. Yu, B.o Liedberg, X. Chen, *Adv. Mater.* **2015**, *27*, 6230.
[11] M. Amjadi, Y. J. Yoon, I. Park, *Nanotechnology* **2015**, *26*, 375501.
[12] S. Y. Hong, Y. H. Lee, H. Park, S. W. Jin, Y.u R.a Jeong, J. Yun, I. You, G. Zi, J. S. Ha, *Adv. Mater.* **2016**, *28*, 930.
[13] A. Miyamoto, S. Lee, N. F. Cooray, S. Lee, M. Mori, N. Matsuhisa, H. Jin, L. Yoda, T. Yokota, A. Itoh, M. Sekino, H. Kawasaki, T. Ebihara, M. Amagai, T. Someya, *Nat. Nanotechnol.* **2017**, *12*, 907.
[14] W. Jeong, J. Song, J. Bae, K. R. Nandanapalli, S. Lee, *ACS Appl. Mater. Interfaces* **2019**, *11*, 44758.
[15] S. Lee, D. Sasaki, D. Kim, M. Mori, T. Yokota, H. Lee, S. Park, K. Fukuda, M. Sekino, K. Matsuura, T. Shimizu, T. Someya, *Nat. Nanotechnol.* **2019**, *14*, 156.
[16] S. Lee, S. Franklin, F. A. Hassani, T. Yokota, M.d O. G. Nayeem, Y. Wang, R. Leib, G. Cheng, D. W. Franklin, T. Someya, *Science* **2020**, *370*, 966.
[17] R. Matsukawa, A. Miyamoto, T. Yokota, T. Someya, *Adv. Healthcare Mater.* **2020**, *9*, 2001322.
[18] Y. Wang, S. Lee, T. Yokota, H. Wang, Z. Jiang, J. Wang, M. Koizumi, T. Someya, *Sci. Adv.* **2020**, *6*, abb7043.
[19] A. Miyamoto, H. Kawasaki, S. Lee, T. Yokota, M. Amagai, T. Someya, *Adv. Healthcare Mater.* **2022**, *11*, 2102425.
[20] W. Wang, M.d O. G. Nayeem, H. Wang, C. Wang, J. J. Kim, B. Wang, S. Lee, T. Yokota, T. Someya, *Adv. Mater. Technol.* **2022**, *7*, 2200479.
[21] W. Du, J. Nie, Z. Ren, T. Jiang, L. Xu, S. Dong, L.i Zheng, X. Chen, H. Li, *Nano Energy* **2018**, *51*, 260.
[22] M. Gong, P. Wan, D.i Ma, M. Zhong, M. Liao, J. Ye, R. Shi, L. Zhang, *Adv. Funct. Mater.* **2019**, *29*, 1902127.
[23] Y. Wang, T. Hong, L. Wang, G. Li, N. Bai, C. Li, P. Lu, M. Cai, Z. Wu, N. Lu, B. Yu, J. Zhang, C. F. Guo, *Mater. Today Phys.* **2020**, *12*, 100191.
[24] W. Jeong, Y. Park, G. Gwon, J. Song, S. Yoo, J. Bae, Y. H. Ko, J.i-H. Choi, S. Lee, *ACS Appl. Mater. Interfaces* **2021**, *13*, 5660.
[25] J. J. Kim, S. Ha, L. Kim, Y. Kato, Y. Wang, C. Okutani, H. Wang, C. Wang, K. Fukuda, S. Lee, T. Yokota, O.h S. Kwon, T. Someya, *Proc. Natl. Acad. Sci.* **2022**, *119*, 2200830119.
[26] Y. J. Fan, X. Li, S. Y. Kuang, L. Zhang, Y. H. Chen, L.u Liu, K.e Zhang, S.i W. Ma, F. Liang, T. Wu, Z. L. Wang, G. Zhu, *ACS Nano* **2018**, *12*, 9326
[27] Z. Jiang, M.d O. G. Nayeem, K. Fukuda, S.u Ding, H. Jin, T. Yokota, D. Inoue, D. Hashizume, T. Someya, *Adv. Mater.* **2019**, *31*, 1903446.
[28] L.u Liu, H. Y. Li, Y. J. Fan, Y. H. Chen, S. Y. Kuang, Z.e B. Li, Z. L. Wang, G. Zhu, *Small* **2019**, *15*, 1900755.
[29] Y. J. Fan, P. T. Yu, F. Liang, X. Li, H. Y. Li, L.u Liu, J. W. Cao, X. J. Zhao, Z. L. Wang, G. Zhu, *Nanoscale* **2020**, *12*, 16053.
[30] W. Jeong, S. Lee, S. Yoo, S. Park, H. Choi, J. Bae, Y. Lee, K. Woo, J.-H. Choi, S. Lee, *ACS Appl. Mater. Interfaces* **2021**, *13*, 60425.
[31] W. Jeong, S. Lee, H. Choi, J. Bae, S. H. Lee, Y. Ma, S. Yoo, J. H. Ha, J.-I.l Hong, S. Park, K. Woo, J.-H. Choi, S. Lee, *Mater. Today* **2022**, *61*, 30.
[32] S. W. Lee, H. J. Lee, J.i H. Choi, W. G. Koh, J. M. Myoung, J. H. Hur, J. J. Park, J. H. Cho, U. Jeong, *Nano Lett.* **2010**, *10*, 347.
[33] H. Kang, D. Kim, S. Baik, *Phys. Chem. Chem. Phys.* **2014**, *16*, 18759.

© 2025 The Author(s). Advanced Materials Interfaces published by Wiley-VCH GmbH

21967350, 2025, 23, Downloaded from https://advanced.onlinelibrary.wiley.com/doi/10.1002/admi.202500600 by Yonsei University Med Library, Wiley Online Library on [13/01/2026]. See the Terms and Conditions (https://onlinelibrary.wiley.com/terms-and-conditions) on Wiley Online Library for rules of use; OA articles are governed by the applicable Creative Commons License

[34] S. Ryu, P. Lee, J. B. Chou, R. Xu, R. Zhao, A. J. Hart, S. G. Kim, *ACS Nano* **2015**, *9*, 5929.
[35] C. Sui, Y. Yang, R. J. Headrick, Z. Pan, J. Wu, J. Zhang, S. Jia, X. Li, W. Gao, O. S. Dewey, C. Wang, X. He, J. Kono, M. Pasquali, J. Lou, *Nanoscale* **2018**, *10*, 14938.
[36] L. Ma, W. Yang, Y. Wang, H. Chen, Y. Xing, J. Wang, *Compos. Sci. Technol.* **2018**, *165*, 190.
[37] D. H. Youn, C. Yeon, J. S. Choi, N. M. Park, I. Lee, G.-H.o Kim, S. J. Yun, *RSC Adv.* **2017**, *7*, 44945.
[38] Y. Yu, Y. Luo, A. Guo, L. Yan, Y. Wu, K. Jiang, Q. Li, S. Fan, J. Wang, *Nanoscale* **2017**, *9*, 6716.
[39] H. Zhang, D. Liu, J. H. Lee, H. Chen, E. Kim, X.i Shen, Q. Zheng, J. Yang, J. K. Kim, *Nano-Micro Lett.* **2021**, *13*, 122.
[40] D. McShan, P. C. Ray, H. Yu, *J. Food Drug Anal.* **2014**, *22*, 116.
[41] B. Zhu, S. Gong, W. Cheng, *Chem. Soc. Rev.* **2019**, *48*, 1668.
[42] S. Chen, Y. Song, D. Ding, Z. Ling, F. Xu, *Adv. Funct. Mater.* **2018**, *28*, 1802547.
[43] J. H. Lee, J. Kim, D. Liu, F. Guo, X.i Shen, Q. Zheng, S. Jeon, J. K. Kim, *Adv. Funct. Mater.* **2019**, *29*, 1901623.
[44] G. Yang, X. Tang, G. Zhao, Y. Li, C. Ma, X. Zhuang, J. Yan, *Chem. Eng. J.* **2022**, *435*, 135004.
[45] C. Li, J. Mu, Y. Song, S. Chen, F. Xu, *ACS Appl. Mater. Interfaces* **2023**, *15*, 9820.
[46] T. Chen, Y. Xie, Z. Wang, J. Lou, D. Liu, R. Xu, Z. Cui, S. Li, M. Panahi-Sarmad, X. Xiao, *ACS Appl. Polym. Mater* **2021**, *3*, 5317.
[47] A. A. Conte, K. Sun, X. Hu, V. Z. Beachley, *Front. Chem.* **2020**, *8*, 610.
[48] W. E. Teo, R. Inai, S. Ramakrishna, *Sci. Technol. Adv. Mater.* **2011**, *12*, 013002.
[49] S. J. Callens, A. A. Zadpoor, *Mater. Today* **2018**, *21*, 241.
[50] J. Lee, G. Yun, J. Jeon, P. T. Le, S. W. Kim, G. Lim, *J. Sens. Sci. Technol.* **2023**, *32*, 335.
[51] S. Duan, Z. Wang, L. Zhang, J. Liu, C. Li, *Adv. Mater. Technol.* **2018**, *3*, 1800020.
[52] Y. Zhou, P. Zhan, M. Ren, G. Zheng, K. Dai, L. Mi, C. Liu, C. Chen, *ACS Appl. Mater. Interfaces* **2019**, *11*, 7405.
[53] S. Zhang, A. Chhetry, M. A. Zahed, S. Sharma, C. Park, S. Yoon, J. Y. Park, *npj Flexible Electron.* **2022**, *6*, 11.
[54] B. J. Kim, E. Meng, *Polym. Adv. Technol.* **2016**, *27*, 564.

© 2025 The Author(s). Advanced Materials Interfaces published by Wiley-VCH GmbH

21967350, 2025, 23, Downloaded from https://advanced.onlinelibrary.wiley.com/doi/10.1002/admi.202500600 by Yonsei University Med Library, Wiley Online Library on [13/01/2026]. See the Terms and Conditions (https://onlinelibrary.wiley.com/terms-and-conditions) on Wiley Online Library for rules of use; OA articles are governed by the applicable Creative Commons License